On dynamo action produced by boundary thermal coupling

Binod Sreenivasan

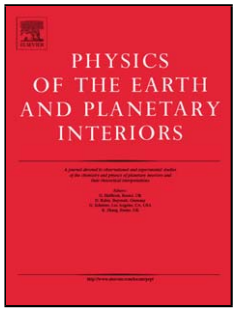

Title: On dynamo action produced by boundary thermal coupling

Author: Binod Sreenivasan

PII: S0031-9201(09)00174-5
DOI: doi:10.1016/j.pepi.2009.08.007
Reference: PEPI 5195

To appear in: *Physics of the Earth and Planetary Interiors*

Received date: 3-10-2008
Revised date: 19-7-2009
Accepted date: 13-8-2009

Please cite this article as: Sreenivasan, B., On dynamo action produced by boundary thermal coupling, *Physics of the Earth and Planetary Interiors* (2008), doi:10.1016/j.pepi.2009.08.007

On dynamo action produced by boundary thermal coupling

Binod Sreenivasan

School of Earth and Environment, University of Leeds, Leeds LS2 9JT, United Kingdom.

Abstract

Rotating dynamos controlled by laterally varying thermal conditions at the boundary are investigated in this paper. A quasi-stationary, locked dynamo solution is obtained when the thermal winds produced by the non-axisymmetric lateral variations come into an approximate balance with the Coriolis forces. This force balance is verified numerically for both equatorially symmetric and antisymmetric boundary variations. The introduction of lateral variations at the boundary can excite dynamo action in a weakly convective regime that does not otherwise sustain a magnetic field with homogeneous boundary heating. A sufficiently large lateral variation drives strong radial and axial fluid motions near the equatorial plane; these flows in turn generate the helicity required for dynamo action. It is shown that a boundary-locked dynamo operates in a state of equipartition between the velocity and magnetic fields. The departure from equipartition in a partially locked dynamo allows the magnetic energy to be greater than the kinetic energy. As the balance of forces in a locked dynamo is different from that in a convection-driven dynamo, lower-mantle coupling could have a marked effect on the structure and dynamics of convection in the Earth's core.

Preprint submitted to Physics of the Earth and Planetary Interiors 19 July 2009

1 Background

Rotating convection and dynamos with fluid-boundary coupling have attracted considerable attention in recent years. The problem is of interest in geophysics where convection in the Earth's outer core is thought to be affected by lateral inhomogeneities in the lower mantle. As the convective turn-over time in the lower mantle is considerably larger than that in the underlying molten core, these lateral variations constitute an approximately static outer boundary condition that could organize core convection in a preferred pattern. Laboratory experiments on rotating, nonmagnetic convection (Sumita & Olson, 1999) showed how a multicolumnar, westward-drifting convection pattern gives way to a locked downwelling front, when a section of the outer boundary is cooled. Numerical studies of rotating convection indicated that a lateral variation in heat flux at the boundary can lock a flow that would otherwise drift (Zhang & Gubbins, 1993). Several dynamo calculations with variable boundary heating (Sarson et al., 1997; Glatzmaier et al., 1999; Olson & Christensen, 2002; Aubert et al., 2007) have presented evidence for a correlation between the magnetic field and boundary thermal anomalies, at least in a time-averaged sense. Recent studies produced, for the first time, dynamos where the magnetic field was nearly locked to lateral variations in heat flux defined by seismic tomography (Gubbins et al., 2007; Willis et al., 2007), enabling direct comparison of a model magnetic field to the present-day geomagnetic field. Although the solution was not stationary, the characteristic four main magnetic flux lobes persisted for many diffusion times at the same sites as the main lobes of the geomagnetic field. These high-latitude magnetic flux concentrations are found to be relatively stationary during the historical period (Bloxham & Gubbins,

Email address: binod@earth.leeds.ac.uk (Binod Sreenivasan).

1985; Jackson et al., 2000) and appear to persist in the time-averaged paleomagnetic field from the past few million years (Johnson & Constable, 1995).

The magnetohydrodynamic (MHD) regime that produces quasi-stationary flux lobes in a dynamo model is significant in two respects: First, it can give insights into the MHD regime that exists in the Earth's liquid iron core. Secondly, lower-mantle effects in the Earth and in different dynamo simulations can be understood with reference to a basic, locked solution. The present paper therefore examines the dynamics of boundary thermal locking in a rotating dynamo. It is shown that the balance of forces in a locked dynamo is fundamentally different from that in a classical, convection-driven dynamo with homogeneous boundary heating. The role of lateral thermal variations in supporting dynamo action under weak buoyancy-driven convection is also investigated for the first time in a computational experiment.

This paper is organized as follows. In Section 2 the governing equations and operating parameters in the model are presented. In Section 3 the dynamics of the locked dynamo are investigated. This includes the behaviour of the energies and lengthscales, the principal force balances and the possible role of the lateral variations in supporting dynamo action. Comparisons with classical dynamos with homogeneous boundary heating are made where appropriate. Finally, in Section 4 the main results of this paper and their implications for the Earth are discussed.

2 The dynamo model

2.1 Governing equations

We consider a thermal convection-driven dynamo where an electrically conducting fluid is confined between two concentric, co-rotating spherical surfaces. The radius ratio r_i/r_o is chosen to be that in the Earth, 0.35. In the Boussinesq approximation, the time-dependent, 3D MHD equations for the velocity $\mathbf{u}$, the magnetic field $\mathbf{B}$ and the temperature T are solved numerically. The governing dimensionless equations are,

$$\frac{E}{Pm}\left(\frac{\partial \mathbf{u}}{\partial t} + (\nabla \times \mathbf{u}) \times \mathbf{u}\right) + \hat{\mathbf{z}} \times \mathbf{u} = -\nabla p^{\star} + Ra\, q\, T\, \mathbf{r} + (\nabla \times \mathbf{B}) \times \mathbf{B} + E\nabla^2 \mathbf{u}, \tag{1}$$

$$\frac{\partial \mathbf{B}}{\partial t} = \nabla \times (\mathbf{u} \times \mathbf{B}) + \nabla^2 \mathbf{B}, \tag{2}$$

$$\frac{\partial T}{\partial t} + (\mathbf{u} \cdot \nabla) T = PmPr^{-1}\, \nabla^2 T + Q_s, \tag{3}$$

$$\nabla \cdot \mathbf{u} = \nabla \cdot \mathbf{B} = 0, \tag{4}$$

where $p^{\star}$ is an augmented fluid pressure that includes the irrotational part of the nonlinear inertial forces and Q_s is a uniform volumetric heat source/sink. The dimensionless groups in Equations (1)–(3) are the Ekman number, $E = \nu/2\Omega L^2$, the Prandtl number, $Pr = \nu/\kappa$, the magnetic Prandtl number, $Pm = \nu/\eta$ and the 'modified' Rayleigh number Ra, whose definition depends on the basic state temperature profile and the thermal boundary condition in the problem. (The various cases considered in this paper are described in Section 2.2.) In the above dimensionless groups, ν is the kinematic viscosity, κ is the thermal diffusivity, η is the magnetic diffusivity, L is the gap-width of the spherical shell and Ω is the angular velocity of rotation. The Roberts number is given by $q = PmPr^{-1}$. The Ekman number is a measure of the

rotation rate and the Rayleigh number represents the strength of convective buoyancy in the problem. As velocity is scaled by η/L, the volume-averaged dimensionless velocity in the model directly gives the magnetic Reynolds number, R_m. The standard numerical method used here involves expanding T and the poloidal and toroidal components of $\mathbf{u}$ and $\mathbf{B}$ in spherical harmonics and then timestepping the spectral coefficients (Sreenivasan & Jones, 2006a). No-slip boundary conditions are imposed on the flow. The inner core is considered to be at a fixed temperature and electrically conducting. The outer boundary is maintained electrically insulating and subject to a lateral variation in temperature or heat flux (see Section 2.2). The variation at the outer boundary is proportional to the spherical harmonic $g(\theta, \phi) = P_l^m(\cos\theta)\cos m\phi$, where l and m are chosen.

2.2 Basic heating modes and boundary variations

In Cases 1–4 of Table 1, convection is driven by the basic state temperature profile $T_0(r) = \beta_i(r_i^2 - r^2)/2$, where r_i is the inner radius and β_i is related to a uniform, dimensional heat source, Q'_s by $\beta_i = Q'_s/3\kappa$. A Y_2^2 harmonic variation in heat flux is imposed on the outer boundary. The modified Rayleigh number for these cases is given by $Ra = g\alpha\beta_i L^3/2\Omega\kappa$, where g is the gravitational acceleration and α is the coefficient of thermal expansion. The ratio of the maximum (peak-to-peak) variation in heat flux to the mean heat flux at the outer boundary gives the lateral inhomogeneity factor, denoted by f.

In Cases 5 & 6 of Table 1, the basic state temperature distribution is one of pure basal heating, $T_0(r) = \beta_b/r$, where $\beta_b = r_i r_o$. A lateral variation in temperature is imposed on the outer boundary. The Rayleigh number for these cases is given by $Ra = g\alpha\Delta T L/2\Omega\kappa$, where ΔT is the basic state temperature

difference across the layer. The ratio of the maximum variation of temperature across the outer boundary to the temperature difference across the layer gives the inhomogeneity factor, f.

In Case 7, a temperature profile that represents a combination of basal heating and intrinsic cooling is considered: $T_0(r) = -\beta_i r^2/2 + \beta_b/r$, where $\beta_b = r_i r_o$ and $\beta_i = -0.25$. A Y_2^2 variation in temperature is imposed on the outer boundary. The Rayleigh number is defined based on the temperature drop across the layer from basal heating alone, and the inhomogeneity factor has the same definition as in Cases 5 & 6.

3 Results

3.1 Flow structures, energies and lengthscales

We begin the study with Cases 1–4 in Table 1 where a Y_2^2 variation in heat flux is applied at the outer boundary. The Ekman number is fixed at $E = 10^{-4}$, for which the onset of thermal convection occurs at $Ra_c \approx 22.8$, where Ra_c is the critical Rayleigh number. The Rayleigh number is fixed at a marginally supercritical value ($Ra \approx 1.5 Ra_c$). Since the convective Rayleigh number is small, the ratio of thermal to magnetic diffusivities, q is set to 10 for possible magnetic field generation. For a lateral inhomogeneity factor $f \leq 0.6$, a multicolumnar flow is present as shown in Fig. 1(a); however, there is no dynamo action. Fig. 2 shows the kinetic and magnetic energies, given by

$$E_k = \frac{1}{2}\int \mathbf{u}^2 dV; \; E_m = \frac{Pm}{2E}\int \mathbf{B}^2 dV. \tag{5}$$

For $f = 0.9$ dynamo action is produced with the magnetic energy being greater than the kinetic energy. As f is increased to 1.6, the amplitude of oscillations in the energy is reduced. The kinetic and magnetic energies are found to be approximately equal (see Fig. 2 and also Table 2). The dominant structure of the flow for $0.9 < f < 1.6$ consists of two static downwellings near $\phi = \pm\pi/2$, as shown in Fig. 1(b) and Fig. 3(a). These strong, narrow downwellings are produced by the azimuthal inhomogeneity in absolute temperature, i.e. the sum of the mean temperature and the lateral variation. For Case 3 in Table 1 ($f = 1.6$) the absolute equatorial temperatures on $r = r_o$ (measured relative to the fixed temperature on $r = r_i$) at $\phi = [0, \pi/2]$ are $[-0.18, -1.18]$. In Case 7 a Y_2^2 variation in temperature is applied on the outer boundary. The respective absolute temperatures for this case are $[0.449, -1.95]$. The narrow downwellings in Fig. 3(a) concentrate the radial magnetic flux in four distinct lobes that are symmetric with respect to the equator, as shown in Fig. 3(b).

Now, the azimuthal lengthscales of the velocity and magnetic field, l_u and l_B, may be estimated from a weighted average of the respective wavenumbers, m, as follows:

$$m_u = \frac{\sum m < u_m^2 >}{\int \mathbf{u}^2 dV}; \; m_B = \frac{\sum m < B_m^2 >}{\int \mathbf{B}^2 dV}, \tag{6}$$

where the angled brackets represent time averages and the sum is over all m. The lengthscales l_u and l_B are given by $2\pi/m_u$ and $2\pi/m_B$. An alternative, 'dissipative' lengthscale for $\mathbf{u}$ and $\mathbf{B}$ is also defined based on the ratio of kinetic energy to viscous dissipation and the ratio of magnetic energy to Ohmic dissipation. The ratio of l_B to l_u in the runs, obtained from (6), is given in Table 2 and the ratio of dissipative lengthscales is given in brackets. It is evident that the lengthscales of $\mathbf{u}$ and $\mathbf{B}$ are approximately equal in the locked regime. Indeed, we find from Fig. 4(a) that the spectra of kinetic and magnetic energies have identical peaks at the boundary-imposed wavenumber $m = 2$ and

its large-scale multiples. The congruence between the lengthscales of $\mathbf{u}$ and $\mathbf{B}$ may further be verified from a contour plot of the radial magnetic field near the equator, which has a structure similar to that of the radial velocity shown in Fig. 1(b). The approximate equivalence of the lengthscales l_u and l_B and the energies E_k and E_m in (5) indicates an equipartition state.

Increasing the inhomogeneity factor, f to > 1.6 causes the magnetic field to weaken considerably, and when $f \approx 2$ the field decays rapidly to zero. For $f = 2.4$ (see Fig. 1(c) and Case 4, Table 1) strong azimuthal flows are produced by the lateral variation, causing the downwellings to be distorted from a radial into a spiral structure, similar to that observed at large f in a laboratory experiment of thermal convection (Sumita & Olson, 1999). Although the precise numerical value of f that results in dynamo failure would depend on the parameters chosen in the model, the above result is significant: where the applied inhomogeneity is either too small or too big, the dynamo fails. From Table 1 we note that the volume-averaged root mean square value of the velocity in the model, $< u >_{rms}$ (which gives the magnetic Reynolds number for a dynamo calculation) increases as f is increased from 0.6 to 2.4 and all other parameters are kept fixed. Yet, dynamo action is lost at $f \sim 2$. We note from Figs. 1(b) & (c) that the transformation from a radial to spiral structure as f is increased is accompanied by a significant decrease in fluid velocity within the downwelling. As we shall see below in Section 3.3, the axial (z) velocity at $f = 2.4$ is also significantly lower than that at $f = 1.6$. This suggests that dynamo action is determined by the magnitude of the velocity within the fluid rolls, rather than the rms value of the velocity.

3.2 Force balances in locking

The spherical surface plot of the azimuthal velocity, u_ϕ for $f = 1.6$ (Fig. 3(c); Case 3 in Tables 1 & 2) may be understood from the temperature distribution imposed by the Y_2^2 boundary variation. At $\phi = \pm\pi/2$, $\partial T/\partial\theta$ is negative in the northern hemisphere, and u_ϕ changes sign from positive (cyclonic) near the equatorial plane to negative (anticyclonic) at high latitudes. The opposite effect is seen beneath warm regions, $\phi = 0, \pi$. An similar pattern of u_ϕ is obtained at every radius of the spherical shell except near the inner boundary ($r = r_i$), indicating that the boundary thermal variation has penetrated the fluid down to the inner boundary. For $f = 1.6$ the equatorial symmetry of the boundary condition is *mapped* on to the velocity field. The symmetry of the locked state forces the net kinetic helicity of the dynamo, $H = \int \mathbf{u}\cdot(\nabla\times\mathbf{u})dV$ to decrease by 8 orders of magnitude from its value at $f = 0.9$, as shown in Fig. 3(d). This suggests that, while the equatorial symmetry of the dynamo solution at $f = 0.9$ is approximate, the symmetry at $f = 1.6$ is exact. (In near-complete locking, the helicities in the two hemispheres are approximately equal in magnitude and of opposite sign.) As the boundary condition appears to control the flow structure in Fig. 3, we first examine the validity of the following thermal wind-type balance in the curl of the momentum equation:

$$\frac{\partial \mathbf{u}}{\partial z} = -Ra\, q\, \nabla \times (T\mathbf{r}), \tag{7}$$

where the temperature gradients are dominated by the non-axisymmetric lateral variations at the boundary, rather than free convection. In Fig. 5 the ϕ-components of the forces in (7) are plotted at longitude $\phi = \pi/2$. For $f = 1.6$ the velocity gradient $\partial u_\phi/\partial z$ follows the local thermal wind $Ra\, q\, (1/r)\, \partial T/\partial\theta$, and the two forces are of the same order of magnitude except in the Ekman

layer at the upper boundary where $\partial u_\phi/\partial z$ is one order of magnitude higher than that in the interior. (The Ekman layer region could not be shown in the same plot because of this large difference in magnitude.) For a weaker inhomogeneity ($f = 0.6$) the thermal wind term is markedly smaller; see Fig. 5(b). The steep gradient $\partial T/\partial\theta$ produced by the Y_2^2 variation for $f = 1.6$ is absent for $f = 0.6$.

The θ-component of (7) in spherical polar coordinates relates the latitudinal velocity, u_θ to the azimuthal gradient in boundary temperature:

$$\frac{\partial u_\theta}{\partial z} = -\frac{Ra\, q}{\sin\theta}\frac{\partial T}{\partial \phi}. \tag{8}$$

For an equatorially symmetric Y_2^2 variation, a positive $\partial T/\partial\phi$ should be correlated to a negative u_θ above the equatorial plane ($z > 0$). This prediction is confirmed in plots of $\partial T/\partial\phi$ and u_θ versus longitude ϕ, shown in Fig. 6(a) for Case 3 in Table 1. The dotted vertical line in this figure gives the longitude at which temperature is minimum. The profiles of u_θ and $\partial T/\partial\phi$ are subject to a small, finite eastward shift from $\phi = \pi/2$ as seen in Fig. 6(a). This azimuthal shift shows up in plots of the radial velocity at a horizontal section near the equator [e.g. Fig. 1(b)]. The correlation between u_θ and $\partial T/\partial\phi$ is strongly evident for a Y_2^2 variation in *temperature* (Case 7 in Tables 1 & 2). Here $\partial T/\partial\phi$ has a smooth $\sin 2\phi$ variation at the outer boundary, but its profile is transformed into a spiked structure by the profile of u_θ beneath the boundary [Fig. 6(b)].

Table 2 summarizes the relative magnitudes of three forces in the momentum equation. We have a rotationally dominant regime in all calculations as the nonlinear inertial forces are small in comparison with the Coriolis forces. This is also confirmed by the small value of the local Rossby number, Ro_ℓ

(Christensen & Aubert, 2006; Olson & Christensen, 2006) defined based on a characteristic lengthscale of the flow. (Here the lengthscale is derived from a typical spherical harmonic degree, ℓ_u obtained as a weighted average from the kinetic energy spectrum). Inertia does play a role in the momentum equation as thermal locking results in an approximate balance between the nonlinear inertial and Lorentz forces:

$$\frac{E}{Pm}\left(\nabla \times \mathbf{u}\right) \times \mathbf{u} \approx \left(\nabla \times \mathbf{B}\right) \times \mathbf{B}, \tag{9}$$

which admits the equipartition solution (see Chandrasekhar, 1961, p 157). The equivalence of the kinetic and magnetic energies in (5) and that of the lengthscales l_u and l_B are consistent with (9). Note that the inertial term increases from 20% to 75% of the Lorentz force term as f is increased from 0.9 to 1.6 for the Y_2^2 variation (compare Cases 2 & 3, Table 2). This result indicates that the balance in (9) is enforced in the locked dynamo regime. The global inertia-Lorentz force balance also holds for the locked solutions subject to Y_8^8 and Y_5^4 variations in temperature at the outer boundary (see Cases 5 & 6, Table 2). The above force balance is absent in convective dynamos with thermally homogeneous boundaries that produce stable, dipolar magnetic fields – for Cases 8 & 9 the inertial forces are much weaker than the Lorentz forces. These dynamos operate in an approximate balance between the magnetic, Archimedean (buoyancy) and Coriolis forces, or the MAC balance (also see Sreenivasan & Jones, 2006a). The magnetic energy for these dynamos is typically higher than the kinetic energy, and the lengthscale of the magnetic field is larger than that of the velocity field. The main differences between boundary-locked dynamos and convection-driven, dipolar dynamos are summarized in Table 3.

To test whether strong thermal coupling can be achieved in a regime of large

Ra and $q \sim 1$, a basic state temperature profile incorporating basal heating and uniform intrinsic cooling is considered in Case 7. (The basic state for this case is given in Section 2.2). Here, thermal convection is weakened as we move from the inner to the outer boundary, allowing the imposed Y_2^2 temperature variation to penetrate into the fluid. Locking is not as rigid as in Case 3, but persistent downwellings similar to those in Figs. 1(b) and 3(c) are recovered. The velocity and magnetic field structures for this case are given in Fig. 5 of a recent paper by the author (Sreenivasan & Gubbins, 2008). While the flow is dominated by the two downwellings, convection rolls tend to migrate towards $\phi = \pm\pi/2$ and clump together near these longitudes. The formation of roll clusters indicates that free convection is not negligible in the thermal wind. The wavenumber of free convection therefore appears in the solution with the wavenumber of the imposed lateral variation. (Also see the discussion on low Ekman numbers in Section 4). From Table 2 we note that the solution in Case 7 departs from equipartition as the ratio of inertial to Lorentz forces is 0.543. Nevertheless, this ratio is much higher than that for a dynamo with homogeneous boundary heating (Case 8).

Table 2 also gives the relative magnitudes of the inductive and diffusive terms in the 'uncurled' induction equation. We find that $(\nabla \times \mathbf{B})$ is systematically smaller than $(\mathbf{u} \times \mathbf{B})$ in the locked solution, as found for dynamos with homogeneous boundaries (Cases 8 & 9).

3.3 The role of boundary thermal anomalies in dynamo action

To focus on the role of the boundary thermal inhomogeneity in dynamo action, a computational experiment is performed with the equatorially symmetric Y_2^2 boundary heating condition. The calculation begins with the locked state at

$f = 1.6$ (see Fig. 7). At time $t_d = 1$, the magnitude of the lateral inhomogeneity is reduced to $f = 0.6$, following which the magnetic energy, E_m falls by three orders of magnitude over one diffusion time. If left to evolve freely, the magnetic field would decay to zero in this phase. However, by setting $f = 1.3$ at $t_d = 2$ and keeping all other parameters the same as before, E_m increases rapidly from its low value and stabilizes at a value comparable to that at $t_d = 0$. The eventual structure of the flow is identical to that in Fig. 1(b), and the locked regime is similar to the one reported in Case 3, Table 1. If the inhomogeneity factor, f is set to 1.6 at $t_d = 2$ [see the dashed curve in Fig. 7(a)], rigid locking is not obtained and E_m saturates at a lower value than at $t_d = 0$. Although the precise value of f at which near-locking is realized is subject to hysteresis, the two locked states obtained in this simulation produce the same energies and lengthscales. It is evident from Fig. 7 that the thermal inhomogeneity at the boundary acts like a "switch" for dynamo action. The inhomogeneity acts on the flow by changing both the axial velocity and vorticity distributions. A sufficiently large lateral variation drives strong axial fluid motions: on azimuthal average, the axial kinetic energy at $f = 1.6$ is concentrated in regions near the equatorial plane which are shown magnified in Fig. 8(a). For too small and too large lateral variations ($f = 0.6$ and $f = 2.4$) the axial energy is distinctly weak. The above effects are reflected in the axial kinetic helicity plotted in Fig. 8(b). While the strong helicity produced for $f = 1.6$ is consistent with dynamo action for this case, the weak helical motions for $f = 0.6$ and $f = 2.4$ do not support dynamo action. The injection of axial energy (and helicity) by the lateral variation is also observed in a nonmagnetic calculation at $f = 1.6$, which indicates that the dynamo magnetic field is mainly supported by boundary-induced helicity. The back-reaction of the magnetic field on the velocity field is small. The effect of the lateral variation

on the sign of vorticity is evident from the behaviour of the axial vorticity skewness, $S = \int \omega_z^3 dV / [\int \omega_z^2 dV]^{3/2}$, a diagnostic commonly used in rotating turbulence (Bartello et al., 1994). The value of S in Fig. 7(b) suggests that anticyclonic (negative) vorticity is dominant for $f = 1.6$, while cyclones and anticyclones are of comparable strength for $f = 0.6$. The source of the preferred negative vorticity for $f = 1.6$ is the Ekman layer at the upper boundary where viscous diffusion of vorticity is fed by the strong axial gradient in velocity. Since anticyclonic z-vorticity is strongly correlated to magnetic field generation in Fig. 7, the vorticity skewness could be a useful flow diagnostic for the onset of dynamo action.

3.4 Different patterns of boundary inhomogeneity

In Cases 5 & 6 of Tables 1 & 2, thermal convection is produced solely by basal heating (see Section 2.2). In Case 5 (Y_8^8 boundary variation) dynamo action is lost for $f < 0.5$. The kinetic and magnetic energy spectra have coinciding peaks at the wavenumber $m = 8$ and its harmonic multiples [Fig. 4(b)], consistent with the approximate equivalence of lengthscales of $\mathbf{u}$ and $\mathbf{B}$ reported in Table 2. In Case 6 the initial state has an equatorially symmetric velocity field and a weak dipolar magnetic field. The equatorially antisymmetric Y_5^4 boundary condition produces a velocity field that locks the magnetic flux lobes beneath cold regions at the boundary, which do not lie at the same longitude in the two hemispheres; see Figs. 9(a) & (b). As the imposed temperature pattern is equatorially antisymmetric, both $\partial T/\partial\theta$ and $\partial u_\phi/\partial z$ have equatorially symmetric distributions at $\phi = \pi/2$ [Fig. 9(c)]. It is also confirmed that the magnitudes of the forces in the thermal wind balance (7) are comparable in the interior of the flow. In Fig. 9(d) the magnetic energy increases continuously

over 5 diffusion times and saturates to within 1% of the kinetic energy, whose variation is small during the calculation. In addition, we note from Table 2 that the lengthscales of **u** and **B** are approximately equal. In short, the main force balances and the equipartition solution hold regardless of the equatorial symmetry of the applied inhomogeneity.

4 Discussion

In this paper we have looked at the dynamics of boundary-locked dynamos. A quasi-stationary, locked solution is obtained when the thermal winds driven by lateral variations at the boundary are in approximate balance with the Coriolis forces in the fluid. The dimensional force balance in the curl of the momentum equation is given by

$$2\Omega\frac{\partial \mathbf{u}}{\partial z} = -g\alpha\,\nabla \times (T\mathbf{r}), \tag{10}$$

which has the same form as the classical thermal wind equation for rotating thermal convection in a Boussinesq fluid (e.g. Sreenivasan & Jones, 2006b), except that the temperature gradients are prescribed by non-axisymmetric (e.g. Y_2^2) lateral variations. This regime may be simulated numerically in a low-Ra, high-q parameter space where buoyancy-driven convection is weak. Equation (10) is significant in that it allows fluid motion of *any wavenumber* to be produced by a prescribed temperature variation at the boundary. Previous studies had suggested that locking occurs when the wavenumber of convection is similar to the wavenumber of the boundary anomalies (Zhang & Gubbins, 1993); and that a small-scale flow could be converted to a large-scale flow by a self-generated magnetic field to make locking possible (Willis et al., 2007). Clearly, neither the matching of wavenumbers nor the presence of a magnetic

field is required for locking produced by the balance in (10).

The secondary force balance in a locked dynamo is between the nonlinear inertial and Lorentz forces, realized approximately in all locked solutions in this paper but generally absent in buoyancy-driven dynamos with homogeneous boundary heating. The inertia-Lorentz force balance is a consequence of locking produced via Equation (10). By virtue of this balance, the locked dynamo operates in a state of equipartition between the velocity and magnetic fields. The equivalence of scaled **u** and **B** fields has been obtained in several astrophysical dynamo models; e.g. Dorch & Archontis (2004); Mininni et al. (2005). These models differ from the present model in two respects: they are non-rotating; and they incorporate a forcing term in the momentum equation that corresponds to a prescribed, globally non-helical, initial velocity field. The analogy between the locked model and the astrophysical models is apparent if we note that the thermal forcing at the boundary acts to create a **u** field which, in turn, brings the **B** field into equipartition. If $E_k \approx E_m$ and $l_u \approx l_B$, the ratio of viscous to Ohmic (resistive) dissipation rates may be shown to be of order $W_V/W_R \sim \nu/\eta = Pm$ (see Table 2 for comparison). As $Pm = qPr \sim 10$ in the locked model, Ohmic dissipation is approximately one order of magnitude smaller than viscous dissipation.

The introduction of lateral variations at the boundary can excite dynamo action for a given Ra–q combination that does not otherwise produce a dynamo with homogeneous boundary heating. While this effect was first noted in Willis et al. (2007), here we have looked at the role of lateral variations in supporting dynamo action. As shown in Figs. 1 & 8, the variations drive strong radial and axial motions which, in turn, can inject the helicity required for amplification of a seed magnetic field.

A locked dynamo driven by lateral variations at the boundary cannot be applied directly to the Earth for two reasons: the geomagnetic field is not rigidly locked to lower-mantle inhomogeneities; and the Earth's dynamo is thought to be powered by thermal and compositional buoyancy in its fluid core. Nevertheless, the locked model provides a useful starting point in understanding core-mantle interaction in Earth-like conditions. How is locking affected by a high convective Rayleigh number and a low Ekman number? If the buoyancy-driven temperature gradients are stronger than the boundary-driven gradients, the velocity field is "decoupled" from the boundary inhomogeneity and free to drift azimuthally. In other words, the thermal wind term in Equation (10) must contain a dominant non-axisymmetric, boundary-driven component to lock the velocity field. This would explain why a weakly convective parameter regime is crucial for obtaining a boundary-locked dynamo.

For Ekman numbers lower than the ones used in this study, locking becomes progressively difficult. Since the critical Rayleigh number for onset of non-magnetic convection increases with decreasing Ekman number ($Ra_c \sim E^{-1/3}$), even a marginally supercritical convective state would generate strong thermal winds that compete with the boundary-driven thermal winds in balancing the Coriolis forces. A preliminary exploration into low Ekman numbers suggests that the flow structure is different from that at higher Ekman numbers: for a sufficiently large Y_2^2 variation in temperature, the flow at $E = 10^{-5}$ is organized in clusters of small-scale rolls near $\phi = \pm\pi/2$, rather than isolated downwellings. For the higher Ekman numbers investigated in this paper, fluid motion is organized into two isolated downwellings as shown in Fig. 1(b). The above difference between high and low-Ekman number flows can be understood as follows. As the contribution of free convection to the thermal wind can be kept small in high-E simulations, the convective wavenumber is to-

tally suppressed by the boundary wavenumber in the locked solution. On the other hand, as free convection becomes significant in the thermal wind in low-E simulations, the convective wavenumber will show up in the solution in addition to the boundary wavenumber. In short, numerical models with relatively large Ekman numbers are needed to demonstrate the validity of the boundary-driven force balance in (10). A systematic study of low-Ekman number dynamos controlled by lateral variations should be possible when faster computers are available.

The calculation in Case 7 produces a partially locked solution even when free convection is not small. This is achieved by suppressing convection in the outer regions through a volumetric heat sink so that boundary-driven thermal winds are allowed to balance the Coriolis forces. [The thermodynamic implications of a heat sink in a model of Boussinesq convection are discussed in Sreenivasan & Gubbins (2008).] The above regime could be relevant to the Earth's dynamo because the departure from equipartition does allow the magnetic energy, E_m to be greater than the kinetic energy, E_k. A comparison of the dynamo in Case 7 with a purely convective, dipolar dynamo suggests that mantle coupling could increase the magnitude of inertial forces in the fluid core. Note, however, that the inertial forces must be much smaller than the Coriolis forces for the Rossby number in the core to be $\sim 10^{-6}$.

Finally, while the results in this paper are valid for individual equatorially symmetric and antisymmetric boundary heating modes, the effect of complex combinations of these modes on the dynamo needs to be investigated. Such a study would give an insight into the effects of the tomographic boundary condition (Masters et al., 1996) constructed based on the Earth's lower-mantle shear wave velocity variation.

Acknowledgement

I thank the referees for their constructive reviews which helped improve this paper. This work has been sponsored by a Research Fellowship (Grant F/00 122/AD) from the Leverhulme Trust, UK. The calculations were performed on the White Rose Grid cluster at the University of Leeds.

References

Aubert, J., Amit, H., & Hulot, G., 2007. Detecting thermal boundary control in surface flows from numerical dynamos, *Phys. Earth Planet. Inter.*, **160**, 143–156.

Bartello, P., Métais, O., & Lesieur, M., 1994. Coherent structures in rotating three-dimensional turbulence, *J. Fluid Mech.*, **273**, 1–29.

Bloxham, J. & Gubbins, D., 1985. The secular variation of the Earth's magnetic field, *Nature*, **317**, 777–781.

Chandrasekhar, S., 1961. *Hydrodynamic and hydromagnetic stability*, Clarendon Press, Oxford.

Christensen, U. & Aubert, J., 2006. Scaling properties of convection-driven dynamos in rotating spherical shells and application to planetary magnetic fields, *Geophys. J. Int.*, **166**, 97–114.

Dorch, S. B. F. & Archontis, V., 2004. On the saturation of astrophysical dynamos: numerical experiments with the no-cosines flow, *Solar Phys.*, **224**, 171–178.

Glatzmaier, G. A., Coe, R. C., Hongre, L., & Roberts, P. H., 1999. The role of the Earth's mantle in controlling the frequency of geomagnetic reversals, *Nature*, **401**, 885–890.

Gubbins, D., Willis, A. P., & Sreenivasan, B., 2007. Correlation of Earth's magnetic field with lower mantle thermal and seismic structure, *Phys. Earth Planet. Inter.*, **162**, 256–260.

Jackson, A., Jonkers, A. R. T., & Walker, M. R., 2000. Four centuries of geomagnetic secular variation from historical records, *Phil. Trans. R. Soc. Lond. Ser. A*, **358**, 957–990.

Johnson, C. & Constable, C., 1995. The time-averaged geomagnetic field as recorded by lava flows over the past 5 Myr, *Geophys. J. Int.*, **122**, 489–519.

Masters, T. G., Johnson, S., Laske, G., & Bolton, H. F., 1996. A shear-velocity model of the mantle, *Phil. Trans. R. Soc. Lond. Ser. A*, **354**, 1385–1411.

Mininni, P. D., Ponty, Y., Montgomery, D. C., Pinton, J.-F., Politano, H., & Pouquet, A., 2005. Dynamo regimes with a nonhelical forcing, *Astrophys. J.*, **626**, 853–863.

Olson, P. & Christensen, U., 2002. The time-averaged magnetic field in numerical dynamos with non-uniform boundary heat flow, *Geophys. J. Int.*, **151**, 809–823.

Olson, P. & Christensen, U., 2006. Dipole moment scaling for convection-driven planetary dynamos, *Earth Planet. Sci. Lett.*, **250**, 561–571.

Sarson, G. R., Jones, C. A., & Longbottom, A. W., 1997. The influence of boundary region heterogeneities on the geodynamo, *Phys. Earth Planet. Inter.*, **101**, 13–32.

Sreenivasan, B. & Gubbins, D., 2008. Dynamos with weakly convecting outer layers: implications for core-mantle boundary interaction, *Geophys. Astrophys. Fluid Dynam.*, **102**, 395–407.

Sreenivasan, B. & Jones, C. A., 2006. The role of inertia in the evolution of spherical dynamos, *Geophys. J. Int.*, **164**, 467–476.

Sreenivasan, B. & Jones, C. A., 2006. Azimuthal winds, convection and dy-

namo action in the polar regions of planetary cores, *Geophys. Astrophys. Fluid Dynam.*, **100**, 319–339.

Sumita, H. & Olson, P., 1999. A laboratory model for convection in earth's core driven by a thermally heterogeneous mantle, *Science*, **286**, 1547–1549.

Willis, A. P., Sreenivasan, B., & Gubbins, D., 2007. Thermal core-mantle interaction: Exploring regimes for 'locked' dynamo action, *Phys. Earth Planet. Inter.*, **165**, 83–92.

Zhang, K. & Gubbins, D., 1993. Convection in a rotating spherical fluid shell with an inhomogeneous temperature boundary condition at infinite Prandtl number, *J. Fluid Mech.*, **250**, 209–232.

Case	Y_l^m	f	Ra/Ra_c	Pr	q	E	ℓ_{max}	N_r	$R_m\,(<u>_{rms})$	Dynamo?
1	Y_2^2	0.6	1.5	1	10	1×10^{-4}	37	60	128.2	No
2	Y_2^2	0.9	1.5	1	10	1×10^{-4}	37	60	177.2	Yes
3	Y_2^2	1.6	1.5	1	10	1×10^{-4}	37	60	212.8	Yes
4	Y_2^2	2.4	1.5	1	10	1×10^{-4}	37	60	240.0	No
5	Y_8^8	0.5	2.3	1	8	5×10^{-5}	64	60	128.4	Yes
6	Y_5^4	1.0	1.5	1	16	5×10^{-5}	64	60	180.6	Yes
7	Y_2^2	2.5	15	5	1	5×10^{-5}	64	60	213.0	Yes
8	–	–	8	10	1	5×10^{-5}	84	96	128.3	Yes
9	–	–	5	1	1	5×10^{-6}	128	128	122.0	Yes

Table 1

Summary of the calculations studied in this paper. Here f is the inhomogeneity ratio, ℓ_{max} is the highest spherical harmonic degree and N_r is the number of radial grid points used in the computation. Where dynamo action is absent, the volume-averaged root mean square value of the velocity is given in place of the magnetic Reynolds number, R_m. The boundary inhomogeneity is in heat flux for Cases 1–4 and in temperature for Cases 5–7. Convection is produced by internal heating in Cases 1–4, by basal heating in 5 & 6 and by a combination of basal heating and internal cooling in 7. Runs 8 & 9 are dynamos with pure basal heating and a homogeneous (constant temperature) outer boundary condition.

Case	E_m/E_k	W_V/W_R	l_B/l_u	$\frac{\text{Inertia}}{\text{Coriolis}}$	Ro_ℓ	$\frac{\text{Inertia}}{\text{Lorentz}}$	$\frac{<\nabla\times\mathbf{B}>_{rms}}{<\mathbf{u}\times\mathbf{B}>_{rms}}$
2	3.675	2.89	1.01 (1.031)	0.049	4.45×10^{-3}	0.21	0.177
3	1.351	7.45	0.85 (1.003)	0.07	5.96×10^{-3}	0.746	0.145
5	0.908	14.6	1.46 (1.287)	0.018	3.19×10^{-3}	1.307	0.235
6	0.99	24.67	1.24 (1.235)	0.011	1.82×10^{-3}	0.785	0.145
7	3.56	1.98	1.56 (1.327)	0.117	10.4×10^{-3}	0.543	0.143
8	25.36	0.885	2.14 (1.51)	0.02	3.26×10^{-3}	0.06	0.191
9	6.79	0.60	2.84 (2.016)	0.02	4.82×10^{-3}	0.02	0.251

Table 2

A summary of the diagnostics investigated for the dynamos in Table 1. Here E_k and E_m are the global kinetic and magnetic energy densities given by (5), W_V is the viscous dissipation given by $Pm\int(\nabla\times\mathbf{u})^2dV$, W_R is the Ohmic (resistive) dissipation given by $(Pm/E)\int(\nabla\times\mathbf{B})^2dV$, l_u and l_B are the lengthscales of the velocity and magnetic fields and Ro_ℓ is the local Rossby number. The inertial forces are given by $(E/Pm)<(\nabla\times\mathbf{u})\times\mathbf{u}>$, Coriolis forces by $<\hat{\mathbf{z}}\times\mathbf{u}>$ and the Lorentz forces by $<(\nabla\times\mathbf{B})\times\mathbf{B}>$, where the angled brackets represent rms values.

	Property	Boundary-locked	Convection-driven
(i)	Time dependence	Quasi-steady ($\frac{\partial}{\partial t} \approx 0$)	In general, time-varying
(ii)	Primary force balance	Boundary-driven thermal wind balance	MAC balance (e.g. Sreenivasan & Jones, 2006a)
(iii)	Ratio of nonlinear inertia to Coriolis forces	$<< 1$	$<< 1$
(iv)	Ratio of nonlinear inertia to Lorentz forces	≈ 1	$<< 1$
(v)	Energies	$E_m \approx E_k$	$E_m > E_k$
(vi)	Lengthscales	$l_B \approx l_u$	$l_B > l_u$

Table 3

A comparative study of (a) locked dynamos controlled by inhomogeneous boundary heating and (b) convection-driven dynamos producing stable, dipolar magnetic fields.

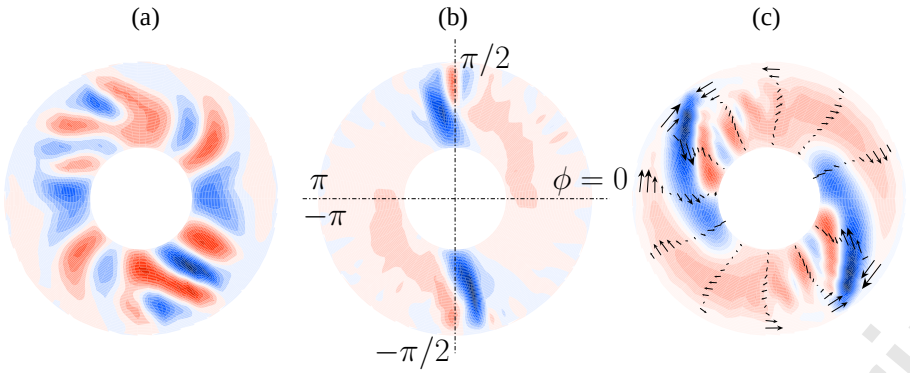

Fig. 1. Equatorial section plots of the radial fluid velocity, u_r for a Y_2^2 heat flux inhomogeneity at the boundary. The three cases studied are (a) $f = 0.6$, (b) $f = 1.6$ and (c) $f = 2.4$. The model parameters are kept fixed for all three cases ($Ra = 1.5Ra_c$, $E = 10^{-4}$, $Pr = 1$ and $q = 10$.) The dimensionless maximum and minimum values for the three cases are $[-284.8, 200]$, $[-654.6, 281.6]$ and $[-215.06, 103.2]$. Positive values of u_r are shown in red and negative values are in blue. Dynamo action is obtained only in (b).

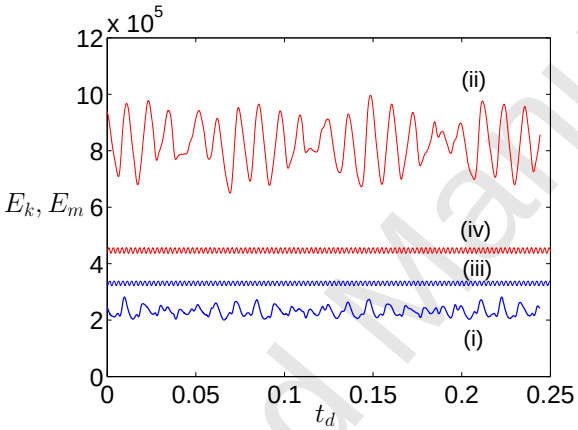

Fig. 2. Kinetic and magnetic energies, E_k and E_m, shown in blue and red curves respectively, over one-fourth of a magnetic diffusion time. Curves (i) and (ii) are for $f = 0.9$ and curves (iii) and (iv) for $f = 1.6$. The model parameters are $Ra = 1.5Ra_c$, $E = 10^{-4}$, $Pr = 1$ and $q = 10$ (Cases 2 & 3 in Table 1).

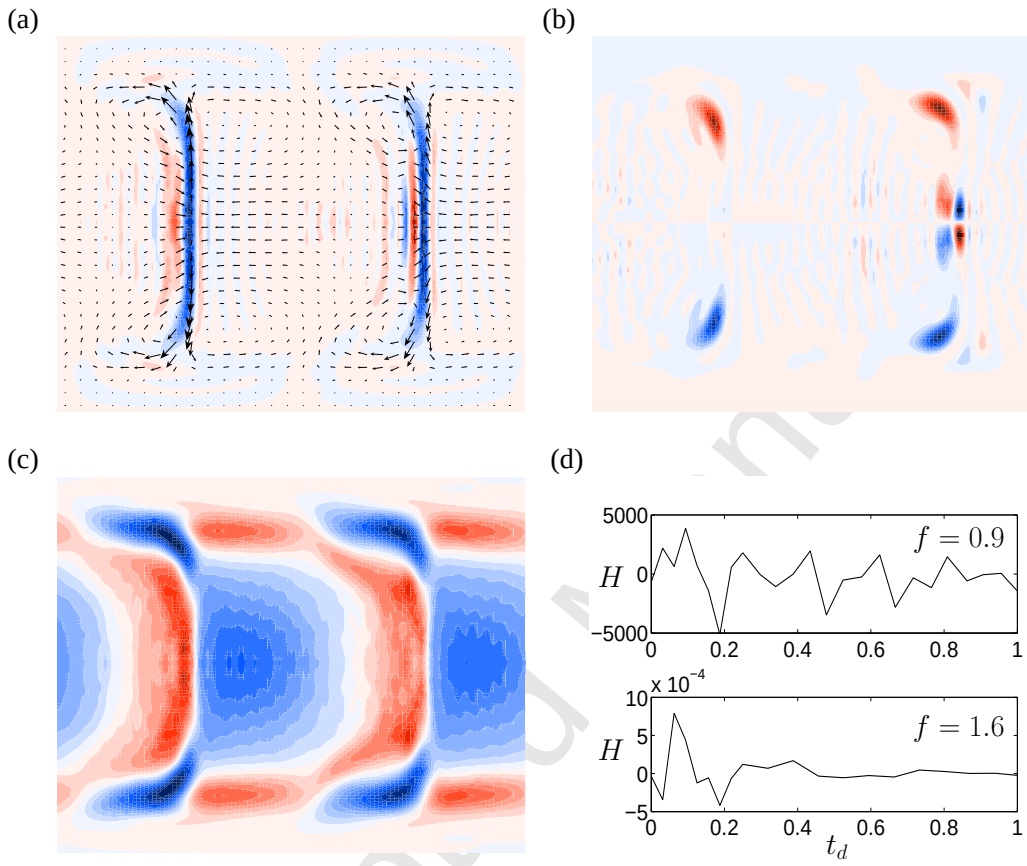

Fig. 3. (a)-(c) are spherical surface plots with longitude ϕ in the range $[-\pi, \pi]$ from left to right on the horizontal axis and colatitude θ in the range $[0, \pi]$ from top to bottom on the vertical axis. (a) $u_r(r = 0.8r_o)$ with surface flow arrows superposed; (b) $B_r(r = r_o)$; (c) $u_\phi(r = 0.8r_o)$, all for a Y_2^2 heat flux variation at $f = 1.6$. Positive values are shown in red and negative values in blue. (d) Global kinetic helicity for $f = 0.9$ and $f = 1.6$. The model parameters are $Ra = 1.5Ra_c$, $E = 10^{-4}$, $Pr = 1$ and $q = 10$.

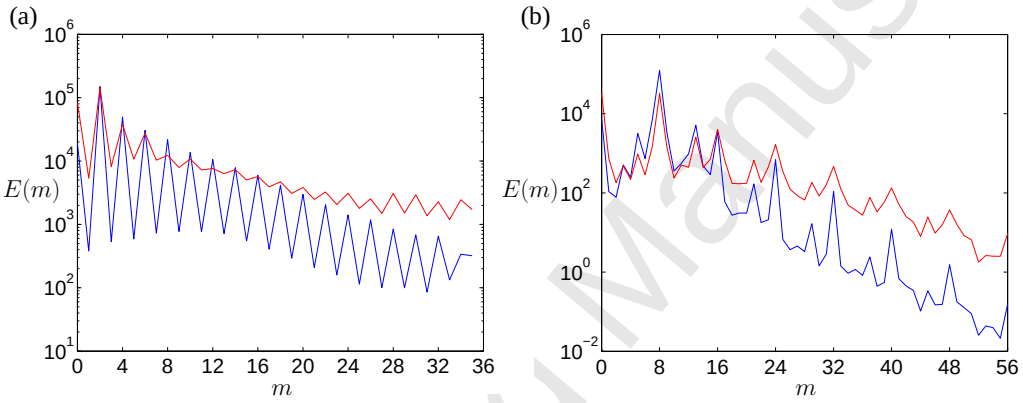

Fig. 4. Spectra of the kinetic and magnetic energies, shown in blue and red curves respectively, as a function of the azimuthal wavenumber, m. (a) Y_2^2 heat flux inhomogeneity (Case 3, Table 1). (b) Y_8^8 temperature inhomogeneity (Case 5, Table 1).

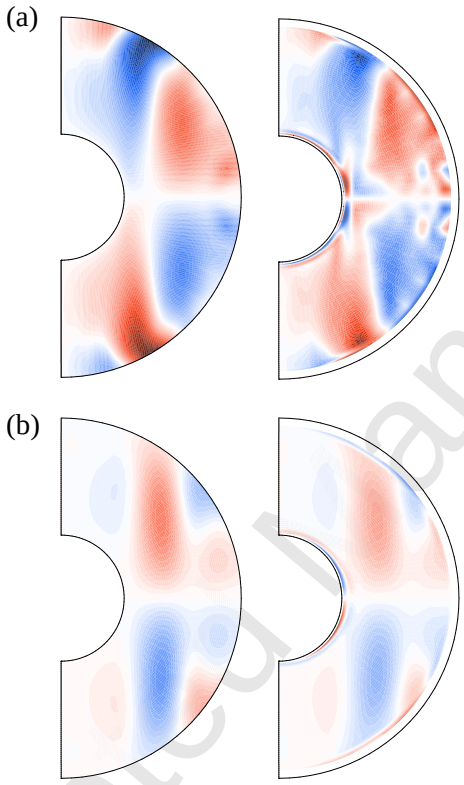

Fig. 5. Meridional plots at azimuthal angle $\phi = \pi/2$ of $Ra\,q\,(1/r)\partial T/\partial\theta$ (left panel) and $\partial u_\phi/\partial z$ (right panel). Two cases are presented for the Y_2^2 heat flux variation: (a) $f = 1.6$ with peak values of the two forces being $[\pm 478.1, \pm 542.8]$; (b) $f = 0.6$ with peak values $[\pm 55.5, \pm 218.9]$. The fixed model parameters are $Ra = 1.5Ra_c$, $E = 10^{-4}$, $Pr = 1$ and $q = 10$. Positive values are shown in red and negative values in blue.

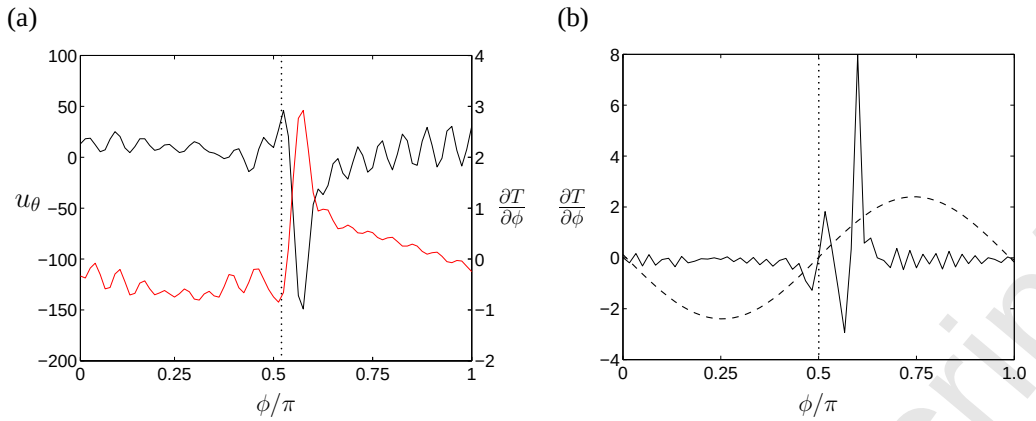

Fig. 6. (a) Dynamo with an imposed Y_2^2 variation in heat flux (Case 3, Table 1) is considered. Latitudinal velocity, u_θ at a horizontal section $z = 0.15$ above the equator and on the spherical surface $r = 0.9r_o$ (black line) and $\partial T/\partial\phi$ at $r = r_o$ (red line) are shown in the range $0 < \phi < \pi$. (b) Dynamo with an imposed Y_2^2 variation in temperature (Case 7). Profiles of $\partial T/\partial\phi$ are shown at $r = r_o$ (dashed line) and $r = 0.9r_o$ (solid line). The dotted vertical lines in the two plots correspond to the longitude where T is minimum at the outer boundary.

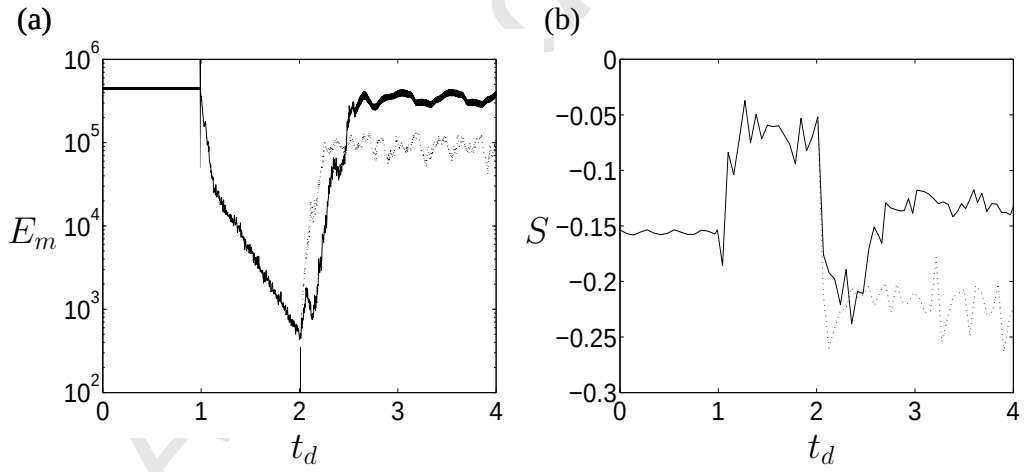

Fig. 7. (a) Variation of the magnetic energy, E_m with magnetic diffusion time. At $t_d = 1$, the inhomogeneity factor, f is switched from its initial value of 1.6 to 0.6. At $t_d = 2$, f is set to 1.3 (solid curve) and 1.6 (dotted curve) in two separate runs. (b) The corresponding variation of the axial vorticity skewness, S. The model parameters are kept fixed at $Ra = 1.5Ra_c$, $E = 10^{-4}$, $Pr = 1$ and $q = 10$.

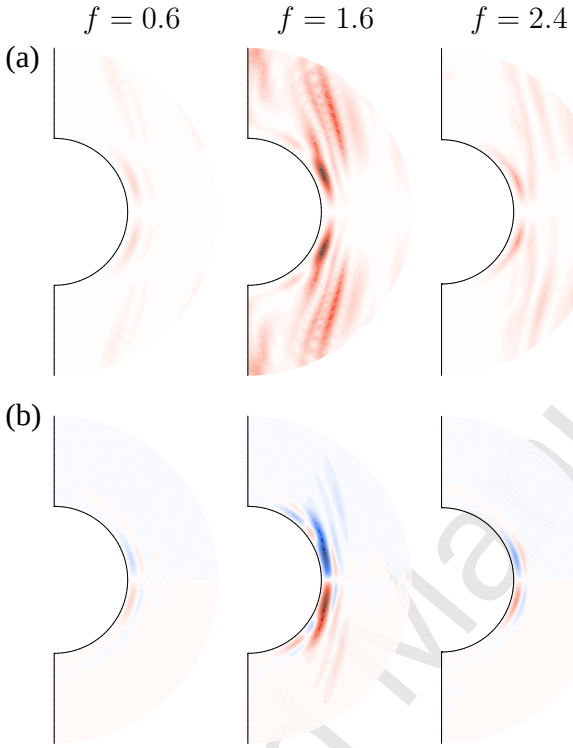

Fig. 8. (a) Meridional contour plots of the axial kinetic energy density, $\frac{1}{2} < u_z^2 >$, where the angled brackets indicate averages over both azimuthal angle, ϕ and time. The region near the inner boundary on either side of the equatorial plane is shown in focus for clarity. The cases presented (from left to right) are $f = 0.6$, $f = 1.6$ and $f = 2.4$ for the Y_2^2 heat flux inhomogeneity. The maximum values of energy for the three cases are 1.3, 19.5 and 2.75 respectively. (b) Contour plots of the axial helicity, $< u_z \omega_z >$. The helicity values in either hemisphere are ± 23.9 ($f = 0.6$); ± 218.3 ($f = 1.6$); ± 64.8 ($f = 2.4$). Positive values are shown in red and negative values are in blue. The model parameters are kept fixed at $Ra = 1.5 Ra_c$, $E = 10^{-4}$, $Pr = 1$ and $q = 10$.

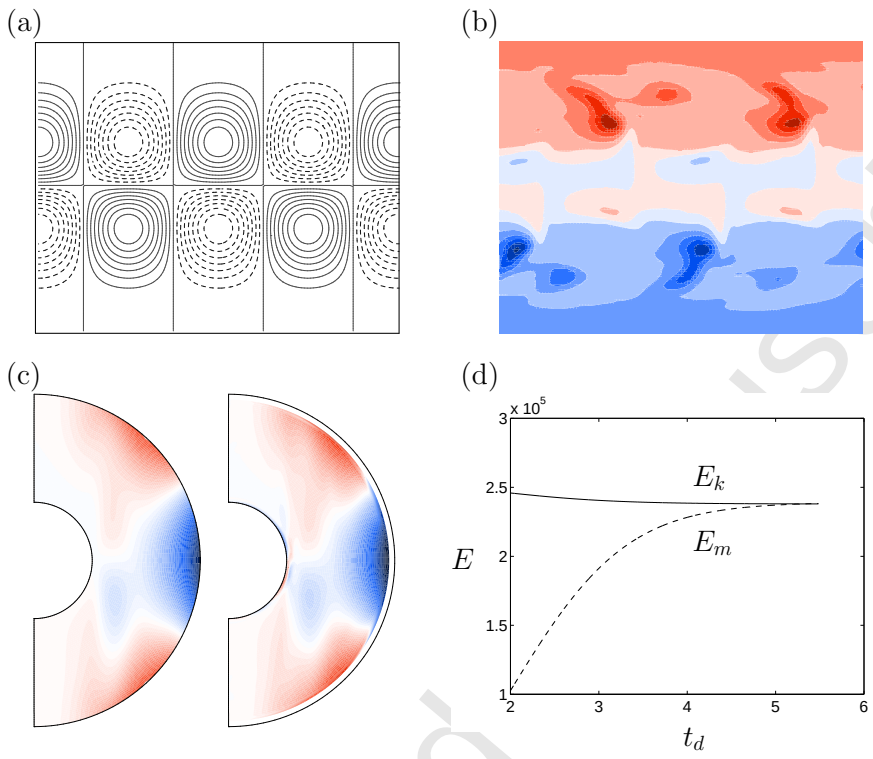

Fig. 9. (a) Spherical surface plot at $r = r_o$ of the applied Y_5^4 temperature variation (Case 6, Tables 1 & 2). The longitude ϕ is in the range $[-\pi, \pi]$ from left to right on the horizontal axis and colatitude θ is in the range $[0, \pi]$ from top to bottom on the vertical axis. Solid lines show positive values and dashed lines show negative values. (b) The locked radial magnetic field distribution at the outer radius. (c) Meridional plots at $\phi = \pi/2$ of $Ra\,q\,(1/r)\partial T/\partial\theta$ (left panel) with minimum and maximum values $[-884.4, 471.1]$; $\partial u_\phi/\partial z$ (right panel) with minimum and maximum values $[-701.1, 473.0]$. Positive values are shown in red and negative values in blue. (d) Evolution of the kinetic energy (solid line) and magnetic energy (dashed line) with magnetic diffusion time.